



Kinetic Model for the Phase Transformation of High-Strength Steel Under Arbitrary Cooling Conditions

Hao Zhao¹ · Xiuli Hu¹ · Junjia Cui² · Zhongwen Xing¹

Received: 24 July 2018 / Accepted: 25 September 2018 / Published online: 11 October 2018
© The Korean Institute of Metals and Materials 2018

Abstract

To meet the demands of energy conservation and security improvement, high-strength steel (HSS) is widely used to produce safety-related automotive components. In addition to fully high-strength parts, HSS is also used to manufacture components with tailored properties. In this work, a computational model is presented to predict the austenite decomposition into ferrite, pearlite, bainite and martensite during arbitrary cooling paths in HSS. First, a kinetic model for both diffusional and martensite transformations under isothermal or non-isothermal with constant cooling rate cooling conditions is proposed based on the well-known Johnson–Mehl–Avrami–Kolmogorov and Kamamoto models. The model is then modified for arbitrary cooling conditions through the introduction of the effects of the cooling rate, and the influence of diffusional transformations on martensite transformation is considered. Next, the detailed kinetics parameters are identified by fitting experimental data from BR1500HS steel. The model is further verified by several experiments conducted outside of the fit domain. The results obtained by calculation are found to be in good agreement with the corresponding experimental data, including the transformation histories, volume fraction microconstituents and Vickers hardness. Additionally, the model is also implemented as a subroutine in ABAQUS to simulate a tailored-strength hot stamping process of HSS, and the results are consistent with the test data. Thus, this computational model can be used as a guideline to design manufacturing processes that achieve the desired microstructure and material properties.

Keywords Kinetic model for phase transformation · HSS · Arbitrary cooling conditions · Microstructure · Hot stamping

1 Introduction

In recent years, the use of high-strength steel (HSS) components has been rapidly increasing in the automotive industry due to needs for higher passive safety and weight reduction [1].

In actual production, hot stamping, hot forging, hot bending, heat treating and welding have been widely used for producing HSS components [2]. In these manufacturing processes, the workpieces are subjected to a thermal cycle that includes heating up and cooling down sections. The microstructures of the final component are formed mainly from the

austenite decomposition in the cooling section. Depending on the temperature history, different phase transformations from austenite into ferrite, pearlite, bainite and martensite will occur [3, 4].

In addition to its use in complete high-strength parts with full martensite, HSS is also used to manufacture some components with tailored properties [4–6] (e.g., a part with different strengths designed in different zones that can adapt to complex load profiles in the event of a collision). These tailored-strength parts are applied in particular to passive automotive safety components.

In general, the material properties for a known chemical composition are determined by the internal microstructures; therefore, it is essential that the final component achieves a desirable microstructure. Hay et al. [7] simulated different stages of the hot stamping process based on a coupling between Pam-Stamp2G and ABAQUS and found that it was crucial to consider the phase change undergone by the part during the quenching phase.

✉ Zhongwen Xing
xzhw@hit.edu.cn

¹ School of Mechanical and Electrical Engineering, Harbin Institute of Technology, Harbin 150001, China

² State Key Laboratory of Advanced Design and Manufacturing for Vehicle Body, Hunan University, Changsha 410082, China

To reduce the trial and error and to obtain savings in both cost and time, it is important to accurately predict the final microstructures of the component early in the product development process [8]. To predict the volume fractions of different phases in HSS accurately, a precise description of the phase transformation kinetics under various circumstances is very important [9].

Based on theory, experimental data or empiricism, several models have been proposed to describe the kinetics of phase transformations in steels. For diffusional transformations, the JMAK model [10–12] and Kirkaldy and Venugopalan (KV) semi-empirical model [13] are the two kinetic models used most frequently. The JMAK model, which is based on nucleation and growth mechanisms, was developed under isothermal cooling conditions, and an additivity rule needs be used to extend the model to non-isothermal cooling conditions. The KV model consists of a series of rate equations depending on the chemical composition. Several authors have made significant efforts to reconstitute these two models to achieve more accurate or convenient predictions of the phase transformation. For instance, the models proposed by Cahn [14], Umemoto [15], Mittermeijer [16], Aarne Pohjonen [17] et al. were developed based on the JMAK model, while the models proposed by Li [18], Åkerström [1], Saunders [19], Lee [20] et al. were based on the KV model. Compared with KV-type models, JMAK-type models require more experimental data and possess greater accuracy; however, they are less convenient. For diffusionless transformations, the KM [21] model is the most commonly used model with reasonable precision. For better accuracy, Magee [22], Tanaka [23] et al. reconstituted this model. Additionally, a new model for martensite transformation developed by Lee [24] in a recent study shows improved accuracy over existing models [4, 20].

Many equations can be developed to describe the kinetics of phase transformation of HSS under arbitrary cooling conditions. However, the reliability of these equations is still under investigation. In this paper, a unified model based on the JMAK and Kamamoto models was proposed to predict both the diffusional and diffusionless phase transformation phenomena that are similar to the measured data. Phase transformation data from BR1500HS steel under isothermal and non-isothermal conditions with a constant cooling rate were recorded from dilatometric testing and hardness tests. In addition, several cooling conditions were designed to verify the accuracy of the kinetic model. For further verification, the model was also implemented as a subroutine in ABAQUS to simulate a tailored-strength hot stamping process of HSS, and the results were compared with the experimental data.

2 Kinetics of Phase Transformation

Ferrite (F) and pearlite (P) transformations are diffusional, while martensite (M) transformation is diffusionless. For bainite (B) transformation, Hehemann, Bhadeshia et al. [25–27] considered it diffusionless (shear mechanism), while Aaronson and Borgenstam [25, 28] believed it was diffusional (diffusion mechanism), and Liu [29] thought it was a shear-diffusion conformity mechanism. However, as the transformation rate is mainly controlled by the diffusion of carbon atoms, bainite transformation kinetics are treated as diffusional [8, 20]. Diffusional transformation involves nucleation and growth mechanisms that are both time and temperature dependent, while the extent of the diffusionless transformation is a function of temperature only.

Among the cooling conditions, isothermal cooling with a certain degree of supercooling from the transformation equilibrium temperature (TTT cooling) and non-isothermal cooling with a constant cooling rate (CCT cooling) are two special and basic types. Except for some special cases in thermomechanical treatments, most of the cooling conditions in common heat treating or processing consist of many substeps in the case of both isothermal and non-isothermal cooling, such as in hot stamping and welding processes, and the cooling rate changes over time. Thus, the phase transformation kinetics for these two basic types of cooling conditions are studied first.

2.1 Kinetics for TTT and CCT cooling conditions

In TTT cooling conditions, the diffusional transformations can be described by the JMAK model [10–12]:

$$X = 1 - \exp(-k \cdot t^n) \quad (1)$$

where X is the volume fraction of the phase at time t . k and n are the kinetic coefficient and exponent, respectively, which are typically functions of the temperature T .

The diffusionless transformation from austenite to martensite can be modelled using the relation proposed by Koistinen and Marburger [21], which is formulated as the following:

$$X_M = X_M^* \cdot (1 - \exp[-\alpha(M_s - T)]) \quad (2)$$

where X_M is the volume fraction of martensite, and X_M^* is the volume fraction of austenite available for the reaction [8]. The factor α is a constant, and $(M_s - T)$ is the supercooling below the martensite start temperature, M_s .

Kamamoto et al. [30] replaced the time t in Eq. (1) with a dimensionless parameter τ as a function of the temperature, as follows:

$$X = 1 - \exp(-k \cdot \tau^n) \quad \text{with } \tau = \frac{T^s - T}{T - T^f} \quad \text{while } T^f < T < T^s \quad (3)$$

where T^s and T^f are the transformation start and finish temperatures. The Kamamoto model can be used for both the diffusional and martensitic transformations in CCT cooling conditions [31]; when $n=1$, Eq. 3 is similar to Eq. 2. In CCT cooling conditions, parameter τ can be defined in the time (or temperature) form as the following:

$$\tau = \frac{t - t^f}{t^f - t^s} = \frac{T^s - T}{T^s - T^f} \quad \text{while} \quad t^f < t < t^s, \quad T^f < T < T^s \quad (4)$$

where t^s and t^f are the transformation start and finish time. The original JMAK equation can be validated only under certain conditions, in particular for continuous nucleation, site saturation, or Avrami nucleation [32] with diffusion-controlled growth or interface-controlled growth. Considering other nucleation (growth) or mixed nucleation (growth) conditions, Eq. (1) can be modified as follows:

$$X = 1 - W * \exp(-k \cdot t^n) - (1 - W) * \exp[-b \cdot t^m] \quad (5)$$

where W is a weighting factor related to the material composition; k and n are the main kinetic coefficient and exponent; and b and m are the accessory coefficient and exponent.

To develop a unified model for both diffusional and diffusionless transformations under either TTT or CCT cooling conditions, a general form based on the JMAK and Kamamoto models can be written as follows:

$$X = X^* \cdot [1 - W * \exp(-k \cdot \tau^n) - (1 - W) * \exp(-b \cdot \tau^m)] \quad (6)$$

where X is the volume fraction transformed; X^* is the volume fraction of austenite available for the reaction. When the cooling rate r_c is below a critical value, martensite

transformation does not occur, and r_c has no impact on X^* ; however, when r_c is large enough, part of the austenite needs to be reserved for martensite transformation. Thus, the cooling rate has a certain impact on X^* in diffusional transformations, as shown in Table 1, where $X_M^{fin}(r_c)$ represents the final volume fraction of martensite under the cooling rate r_c ; X_F , X_{FP} and X_{FPB} represent the transformed volume fractions of F, F + P and F + P + B in arbitrary cooling conditions, respectively and are equal to the final volume fractions X_F^{fin} , $X_F^{fin} + X_P^{fin}$ and $X_F^{fin} + X_P^{fin} + X_B^{fin}$ in TTT and CCT cooling conditions.

2.2 Kinetics for Arbitrary Cooling Conditions

2.2.1 The Start Time of Phase Transformation

The additivity rule proposed by Scheil has been widely used for decades in calculating the start time of diffusional phase transformations under arbitrary cooling conditions using TTT data. The rule of additivity can be represented by the following [33–36]:

$$\int_0^{t^{sA}} \frac{dt}{t^s(T)} = 1 \quad (7)$$

where t^{sA} and $t^s(T)$ are the start time of phase transformation in arbitrary cooling conditions and the isothermal temperature T , respectively. Figure 1a shows a schematic representation of the Scheil additivity rule in which the cooling curve is divided into several isothermal condition substeps with different temperatures, and then, the isothermal incubation rates

Table 1 Reserved volume fraction for each phase transformation

Phase transformation	A → F	A → P	A → B	A → M
X^*	$1 - X_M^{fin}(r_c)$	$1 - X_F - X_M^{fin}(r_c)$	$1 - X_{FP} - X_M^{fin}(r_c)$	$1 - X_{FPB}$

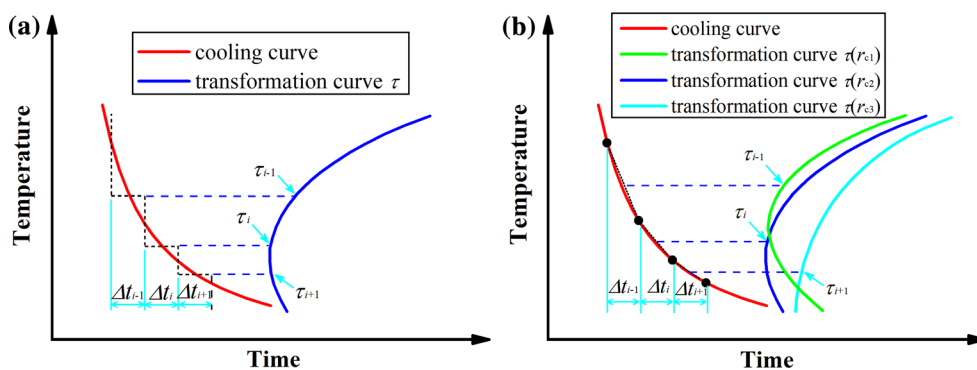


Fig. 1 Schematic representation of the Scheil additivity for predicting the non-isothermal transformation from: **a** TTT data **b** both TTT and CCT data

($\Delta t/t^s(T)$) of each substep are summed incrementally. When Eq. 7 is satisfied, the phase transformation begins. Obviously, the cooling rate r_c , which is one of the key factors controlling the transformation during arbitrary cooling conditions, has not yet been considered in each substep. As stated earlier, arbitrary cooling conditions consist of many substeps for both TTT and CCT cooling conditions. Thus, for better accuracy, the additivity rule can be modified as the following:

$$\int_0^{t^{sA}} \frac{dt}{t^s(r_c, T)} = 1 \tag{8}$$

where $t^s(r_c, T)$ is the start time of the phase transformation in the CCT cooling condition with r_c ($r_c \neq 0$) or in the TTT cooling condition with T ($r_c = 0$). Figure 1b shows a schematic representation of the modified Scheil additivity rule in which the cooling curve is divided into several substeps for different TTT or CCT cooling conditions.

With the permission of the cooling rate and temperature, ferrite transformation occurs first, followed by pearlite transformation and finally bainite transformation. The conditions that need to be met for the start of each diffusional transformation are listed in Table 2, where $t_F^s(r_c, T)$ and $t_B^s(r_c, T)$ are the start time of F and B transformation in the CCT cooling condition with r_c ($r_c \neq 0$) or in the TTT cooling condition with T ($r_c = 0$); Ae_1 and Ae_3 are the equilibrium temperatures; and T_F^D and T_P^D are the death temperatures for ferrite and pearlite transformations, respectively. The first time (or temperature) that satisfies these conditions is simply the start time (or temperature) for the transformation in an arbitrary cooling process.

For martensite transformation, the transformation starts when the temperature cools down to M_s (martensite starting temperature). In CCT cooling conditions, M_s is a constant, M_{s0} , when the cooling rate r_c is greater than the critical value that results in fully martensite (r_{cM1}) transformation; M_s declines with a decrease in the cooling rate when r_c is between the critical values that result in fully martensite (r_{cM1}) and no martensite (r_{cM0}) microstructures. The variation in M_s comes mainly from the enriched carbon content of the austenite due to the diffusional transformations.

Table 2 Conditions for the beginning of each diffusional transformation

Phase transformation	Conditions that need to be met
A → F	(1) $\int_0^{t_F^{sA}} \frac{dt}{t_F^s(r_c, T)} \geq 1$; (2) $T_F^D \leq T \leq Ae_3$; (3) $X_F^{fin}(r_c) > 0$
A → P	(1) $T_P^D \leq T \leq Ae_1$; (2) F transformations has accomplished ($X_F \geq X_F^{fin}(r_c) \neq 0$); (3) $X_P^{fin}(r_c) > 0$
A → B	(1) $\int_0^{t_B^{sA}} \frac{dt}{t_B^s(r_c, T)} \geq 1$; (2) $M_s \leq T \leq Ae_1$; (3) F and P transformations have accomplished or not started

Thus, M_s depends on the whole volume fraction of the diffusional transformations X_D ($X_D = X_F + X_P + X_B$). That is, when $X_D = 0$, $M_s = M_{s0}$; when $X_D > 0$, M_s is a function of X_D and decreases with an increase in X_D .

2.2.2 The Volume Fraction of Phase Transformation

Based on the transformation kinetics under TTT and CCT cooling conditions, the diffusional phase volume fractions X at the current time step t_{p+1} can be calculated as follows:

$$X = X^* \cdot (1 - W \cdot \exp[-k \cdot (\tau^* + d\tau)^n] - (1 - W) \cdot \exp[-b \cdot (\tau^* + d\tau)^m]) \tag{9}$$

where τ^* is an equivalent progress factor at the current time step and can be calculated according to the volume fraction X in the previous time step t_p using Newton’s iteration method. $f(\tau^*) = X - X^* \cdot (1 - W \cdot \exp[-k \cdot (\tau^* + d\tau)^n] - (1 - W) \cdot \exp[-b \cdot (\tau^* + d\tau)^m]) = 0$ is the function in which the root needed to be solved, and $\tau_0^* = 0.5$ is the initial approximation of τ^* . The result of the $(NR + 1)$ th iteration can be expressed by the (NR) th approximation of τ^* as the following:

$$\tau_{NR+1}^* = \tau_{NR}^* - \frac{2 - 2X/X^* - \exp(-b\tau_{NR}^{*m}) - \exp(-k\tau_{NR}^{*n})}{bm\tau_{NR}^{*m-1} \exp(-b\tau_{NR}^{*m}) + kn\tau_{NR}^{*n-1} \exp(-k\tau_{NR}^{*n})} \tag{10}$$

The volume fraction of martensite transformation under arbitrary cooling conditions can be calculated directly using the general form Eq. 6 for CCT cooling conditions. Similar to the calculation of M_s , the diffusionless kinetics depend on the total volume fraction of the diffusional transformations X_D rather than on the temperature or the cooling rate history. In this condition, X_D can be used for the reverse solution of the equivalent cooling rate r_c^{eq} and the related model parameters for CCT cooling conditions. That is, when $X_D = 0$, $r_{cM}^e = r_{cM1}$; when $X_D = 1$, $r_{cM}^e = r_{cM0}$; and when $0 < X_D < 1$, $r_{cM0} < r_{cM}^e < r_{cM1}$.

Figure 2 shows the process of calculating the volume fraction for phase transformations under arbitrary cooling conditions, where e_D is the incubation rate increment, and E_D is the incubation rate for diffusional transformations; dX is the volume fraction increment; $X^{fin}(r_c)$ is the final volume fraction of each phase under the cooling rate r_c ; T_F^{cr}, T_P^{cr} and T_B^{cr} represent the minimum temperature for ferrite transformation, the minimum temperature for pearlite transformation and the maximum temperature for bainite transformation, respectively.

3 Identification of Kinetics Parameters for BR1500HS Steel

Under either TTT or CCT cooling conditions, the process of diffusional and diffusionless transformations can be divided into two parts, as shown in Fig. 3, the preparatory stage (AB

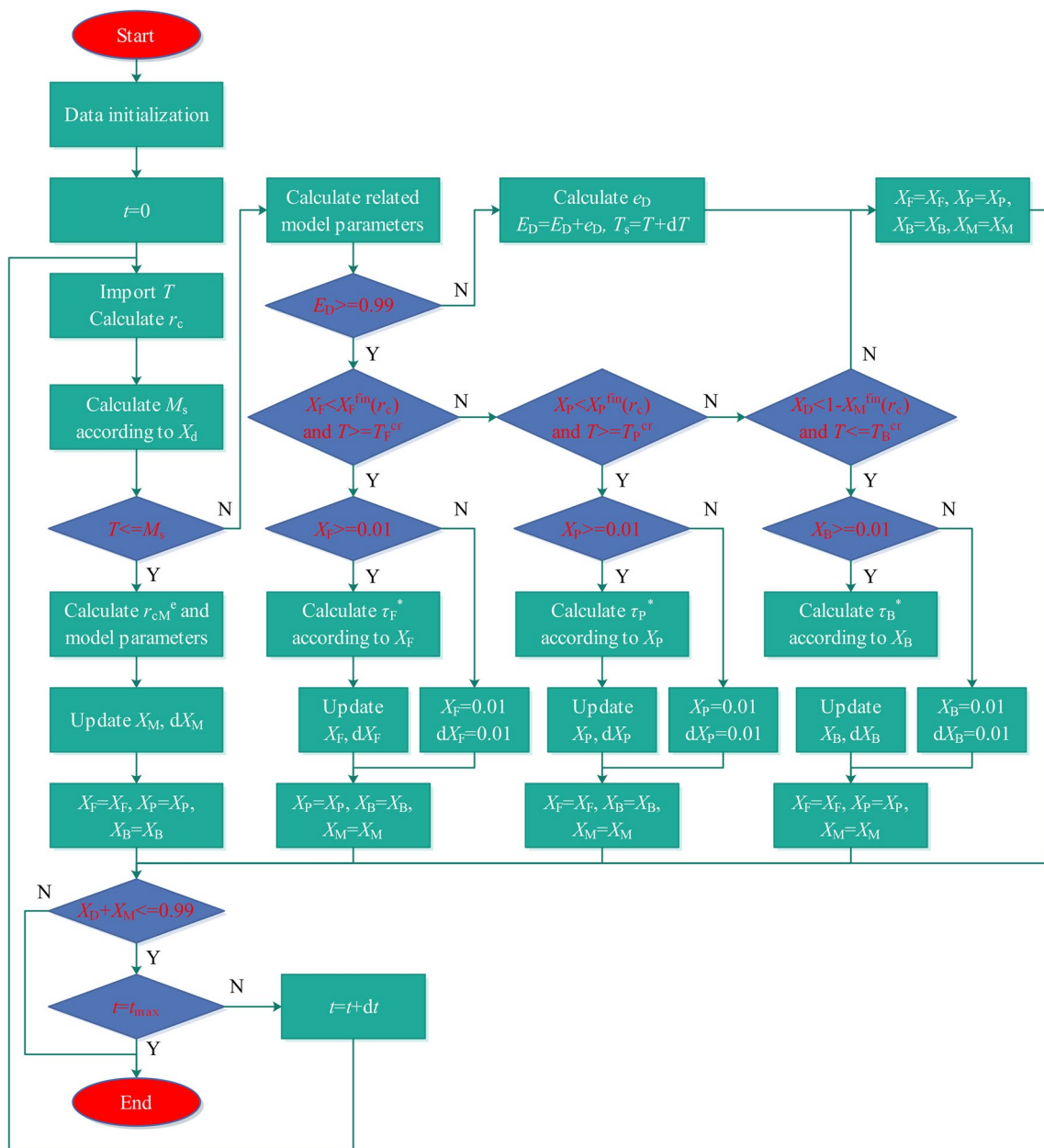
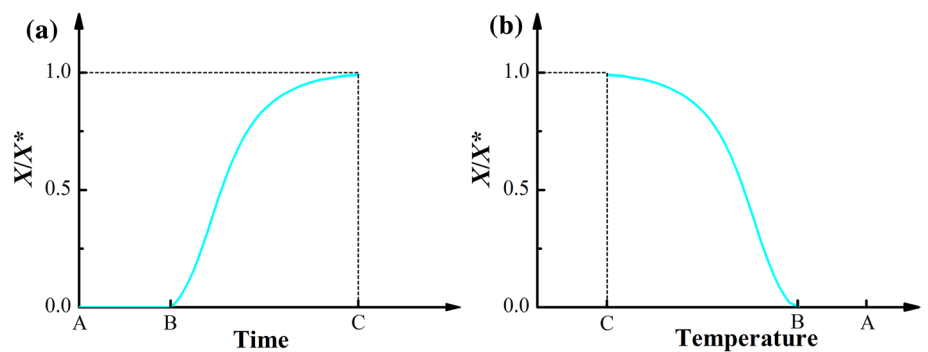


Fig. 2 Process of calculating the volume fraction for phase transformations under any cooling conditions

Fig. 3 The process of phase transformation: **a** Diffusional transformation and **b** diffusionless transformation



segment) and the S-shaped transforming course (BC segment, as the transformation history appears as an ‘S’ curve).

Points A, B and C on the horizontal axis stand, respectively, for the moments at the equilibrium, start and finish temperatures of the diffusional transformations, as well as for the corresponding temperatures of the diffusionless transformations.

Obviously, the mathematical descriptions of the preparatory stage and the S-shaped transforming course constitute the main body of the overall transformation kinetics. Thus, experimental data and curve fitting methods focusing on these two stages will be used to solve and verify the kinetics parameters in this section.

3.1 Material and Experimental Procedure

22MnB5 boron-alloyed steel is a common steel widely used in hot stamping to produce ultra-high-strength automotive parts. Baosteel’s BR1500HS has almost the same chemical composition as this steel grade. The microstructure of the blank in the as-received condition consists of 78 vol% ferrite and 22 vol% pearlite [37, 38]. In this paper, BR1500HS was studied, and the chemical composition is given in Table 3.

The volume fraction of the phase transformation was mainly monitored by the length change due to the thermal expansions using a “Baehr DIL 805A\D” dilatometer. The specimen (10 mm × 3.0 mm × 5.0 mm) was heated up to the austenization temperature (930 °C in this paper), was held for 4 min, and then

- cooled rapidly to several specified temperatures and held for a period of time to obtain TTT cooling conditions;
- cooled to room temperature using several constant rates to obtain CCT cooling conditions; or

- cooled to room temperature at two or three different cooling rates to obtain arbitrary cooling conditions.

In addition to the dilatometry tests, metallographic investigations and hardness measurements were also carried out to further confirm the volume fraction of each phase transformation.

3.2 TTT and CCT Data

TTT and CCT diagrams are constructed by connecting the transformation start times and finish times with separate lines on a temperature versus time diagram. Additionally, the other times of a specified volume fraction can be connected into curves and added to the diagrams. Thus, these two diagrams can be readily used to describe the preparatory stage and S-shaped transforming course.

From the thermal expansion tests, several expansion curves during the TTT and CCT cooling processes are shown in Fig. 4. Austenite is face-centred cubic (FCC) in structure, while ferrite, pearlite, bainite and martensite are body-centred cubic (BCC). Thus, austenite has the minimum specific volume. For the expansion of the specimen caused by austenite decomposition, turning points appear on the expansion curves at the start and end times of each phase transformation.

The lever rule was applied to obtain the overall fraction transformed without considering the carbon enrichment of austenite [39], as shown in Fig. 5 (to avoid clutter from the overlapping of different curves, only part of the transformation histories is plotted).

The cooled specimens were first tested to determine their micro-Vickers hardness and were then etched with 4% nital and examined by optical microscope to identify existing phases. From both the judgement of the turning point on

Table 3 Chemical compositions of BR1500HS steel as-received (wt%)

C	Mn	Cr	Ti	Al	Si	P	S	B	Fe
0.23	1.2	0.25	0.04	0.04	0.4	0.02	0.015	0.002	bal.

Fig. 4 Thermal expansion versus **a** time and **b** temperature during TTT and CCT cooling processes

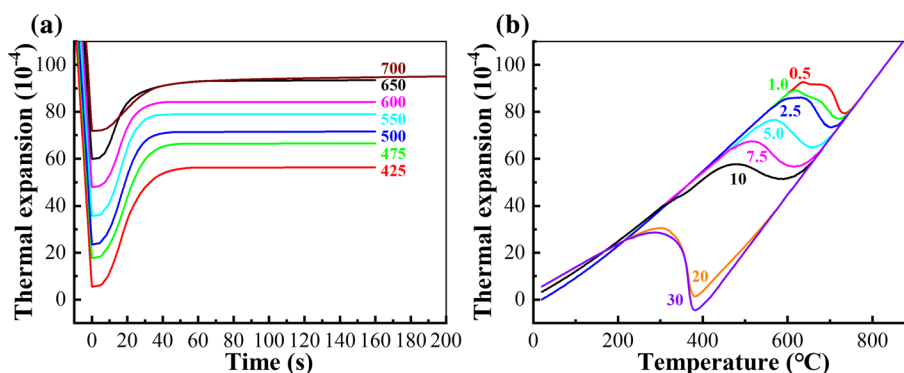
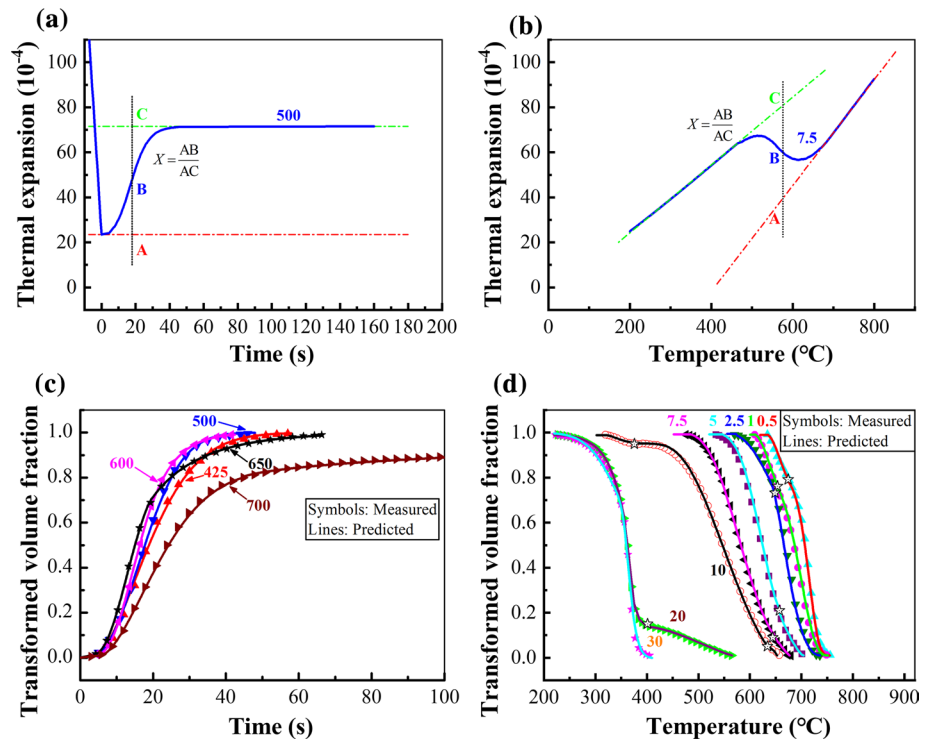


Fig. 5 Conversion from thermal expansion versus **a** time and **b** temperature to transformation volume fraction versus **c** time and **d** temperature by applying the lever rule



the phase transformation history curves and the quantitative metallographic analysis (point analysis method), the final volume fraction X^{fin} for each phase transformation in TTT and CCT cooling conditions was determined, as shown in Fig. 6.

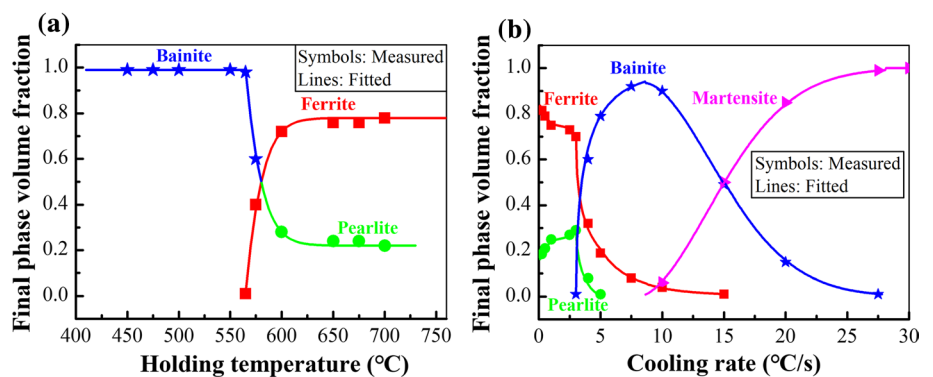
Then, the start and finish times (or temperatures) for each phase transformation in TTT (or CCT) cooling conditions were measured, and the TTT and CCT diagrams for BR1500HS steel are plotted in Fig. 7 with the austenitizing temperature of 930 $^{\circ}\text{C}$.

For diffusional transformations, the transformation start time at each temperature (in TTT) or under each cooling rate (in CCT) represents the preparatory stage. Pham’s model [40–42] was used to describe the start or finish transformation C curves in the experimental TTT diagram. Exponential,

polynomial and some other simple functions were used to describe the start and finish transformation curves for the CCT test results, as shown in Table 4. The fitting curves were in excellent agreement with the measured curves (Fig. 7). The fitting curves of X^{fin} in TTT and CCT cooling conditions were also consistent with the measured values (Fig. 6).

Then, model parameters k , n and b were solved not just by using the starting and finishing volume fractions and corresponding times, as mentioned in many previous studies [43] but also by curve fitting and optimizing the curves as simple functions of the cooling rate r_c or temperature T according to the phase volume fraction versus time curves under different cooling rates for CCT cooling conditions and under different temperatures for TTT cooling conditions. To assure that the final volume fraction X^{fin} appears at the finish time when

Fig. 6 Final resulting phase fractions in **a** TTT and **b** CCT cooling rate conditions



$\tau = 1$, the following formula must be satisfied during the fitting process.

$$b = -\ln\left(\frac{1 - W * \exp(-k) - X^{fin}/X^*}{(1 - W)}\right) \quad (11)$$

Figure 8 shows several model parameters determined by data fitting and optimization. During the fitting process for all the data from the transformation volume fraction versus time (temperature), 0.5 was the optimal value for the weighting factor W . $m = n - 1$ for the diffusional transformations, while $m = n - 3$ for the martensite transformation. In TTT cooling conditions, k and b change with the temperature and

Fig. 7 Transformation diagrams of the BR1500HS steel: **a** TTT and **b** CCT

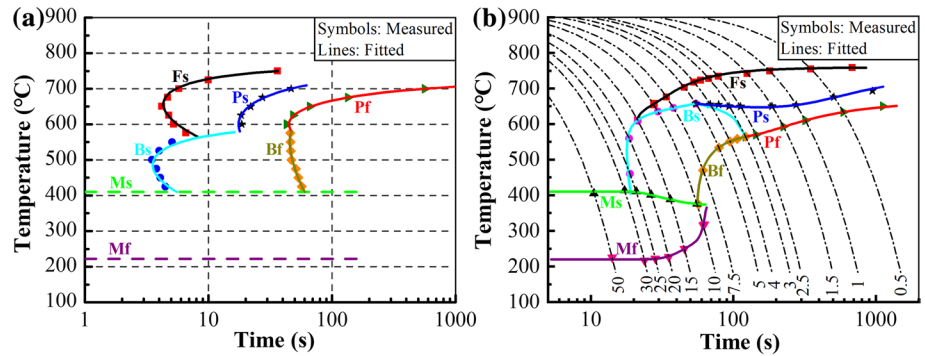


Table 4 Fitting expressions of the start and finish transformation curves in TTT and CCT diagrams

Trans. curve	Time in TTT (s)	Temperature in CCT (°C)
F_s	$\frac{0.4023 * \exp(6913/T)}{(765-T)^{1.74}}$	$-0.007597 * r_c^4 + 0.2333 * r_c^3 - 2.103 * r_c^2 - 5.167 * r_c + 758$ ($0 < r_c \leq 15$)
P_s	$\frac{582.2 * \exp(5075/T)}{(765-T)^{2.342}}$	$103.1 * \exp(-2.217 * r_c) + 638.4 * \exp(0.005872 * r_c)$ ($0 < r_c \leq 5$)
B_s	$\frac{7.678 * \exp(3317/T)}{(600-T)^{1.604}}$	$710 - 145.5 * \exp[-0.8152 * (r_c - 3)^{0.3084}]$ ($3 < r_c \leq 5$) $-0.02779 * r_c^3 + 0.8164 * r_c^2 - 11.99 * r_c + 700.3$ ($5 < r_c \leq 27.5$)
F_f	P_s	P_s ($0 < r_c \leq 5$) B_s ($5 < r_c \leq 15$)
P_f	$\frac{104.2 * \exp(8622/T)}{(730-T)^{3.125}}$	$-0.9333 * r_c^3 + 13.9 * r_c^2 - 66.22 * r_c + 663.26$ ($0 < r_c \leq 3$) B_s ($3 < r_c \leq 5$)
B_f	$\frac{20.08 * \exp(687.6/T)}{(600-T)^{0.11}}$	$-0.1114 * r_c^3 - 0.4129 * r_c^2 - 6.487 * r_c + 590.7$ ($3 < r_c \leq 10$) M_s ($10 < r_c \leq 27.5$)
M_s	410	$8.296 * \exp(-5.772 * X_D) + 402.4 * \exp(-0.07468 * X_D)$ ($8.5 < r_c \leq 27.5$) 410 ($27.5 < r_c$)
M_f	220	$219.9 * \exp(0.249 * X_D) + 0.0001785 * \exp(13.16 * X_D)$ ($8.5 < r_c \leq 27.5$) 220 ($27.5 < r_c$)

Fig. 8 Model parameters gained by data fitting and optimization in **a** TTT and **b** CCT cooling conditions

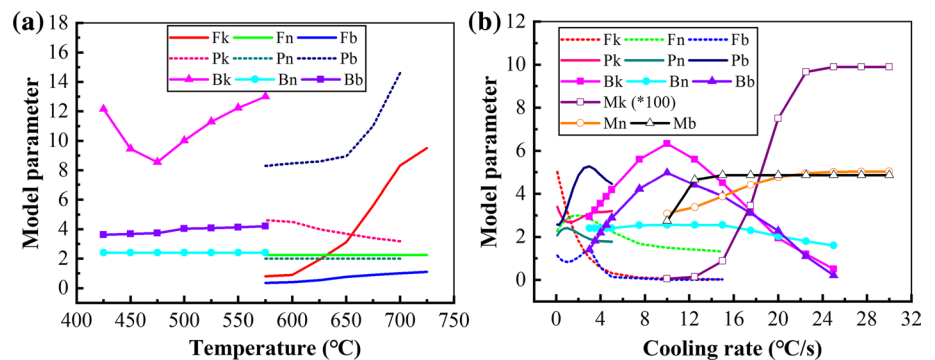
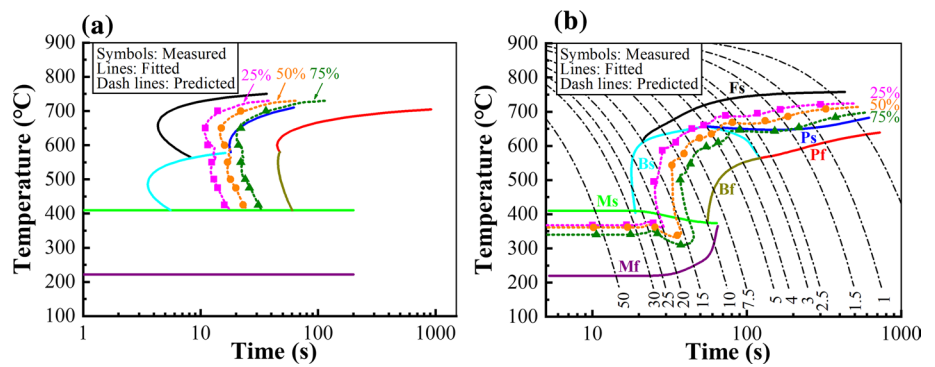


Fig. 9 The predicted and measured curves corresponding to 25%, 50% and 75% transformation in **a** TTT and **b** CCT diagrams



n remains unchanged; in CCT cooling conditions, k , n and b change with the cooling rate. In addition, when the cooling rate r_c is close to 0 in CCT cooling conditions, the value of n is also close to the corresponding value in TTT cooling conditions.

Finally, these model parameters were returned to the kinetic model, and the phase transformation histories were predicted, as shown in Fig. 5. Figure 9 shows the predicted and measured curves corresponding to 25%, 50% and 75% transformation in the TTT and CCT diagrams. In general, the simulated curves were in excellent agreement with the measured curves.

In addition, the final strength expressed by the Vickers hardness (HV) can be estimated as a function of the hardness of the individual phases and the resulting phase volume fractions as follows [8, 44]:

$$HV|_{n+1} = HV|_n + \sum_{i=2}^5 ((X_i|_{n+1} - X_i|_n) \cdot [H_i(r_c) - H_1(r_c)]) \tag{12}$$

where $i = 1, 2, 3, 4$ and 5 represent austenite (A), ferrite (F), pearlite (P), bainite (B) and martensite (M) transformations, respectively; X_i is the volume fraction of each phase; and $H_i(r_c)$ is the Vickers hardness at room temperature for individual phases of BR1500HS, which change with the cooling rate r_c for phase transformation, as shown in Fig. 10. Based on the predicted phase volume fractions, the final Vickers hardness for different cooling rates for CCT cooling conditions was calculated, and the result is consistent with the measured values.

3.3 Model Validation

To further verify the performance of the developed phase transformation model, several cooling paths from 930 °C under various rates, as plotted in Fig. 11, were designed according to Sect. 3.1, and the corresponding evolutions of the phase volume fractions and Vickers hardness were simulated. Cooling paths 2 and 3 represent natural cooling under vacuum and ventilation cooling, respectively.

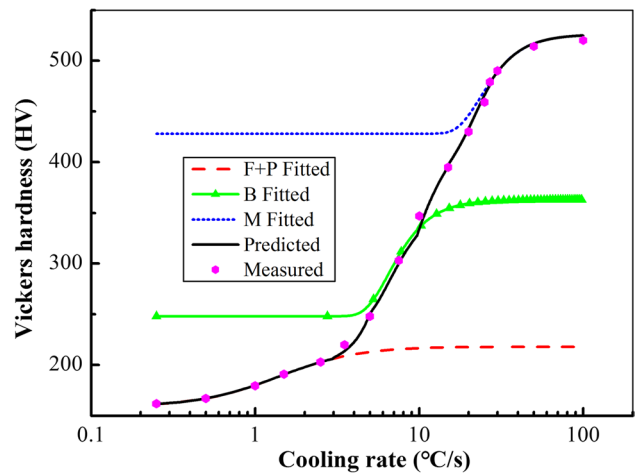


Fig. 10 The fitted, predicted and measured Vickers hardness under different cooling rates

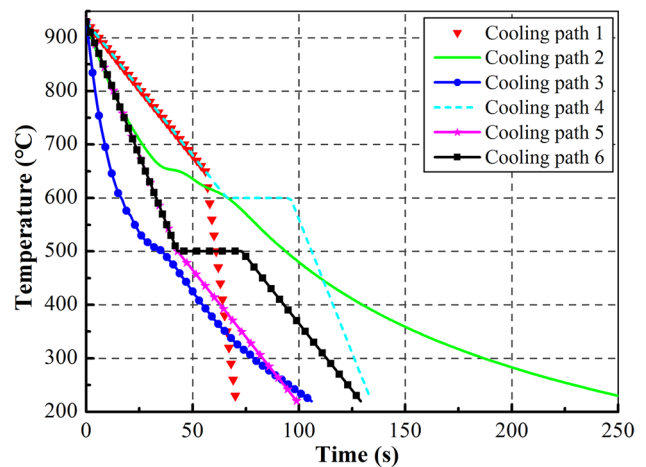


Fig. 11 Several cooling paths under various rates

During the calculation, the prescribed time increment Δt was set to 0.5 s for each time step, and cooling rates less than 0.1 °C/s were treated as isothermal conditions.

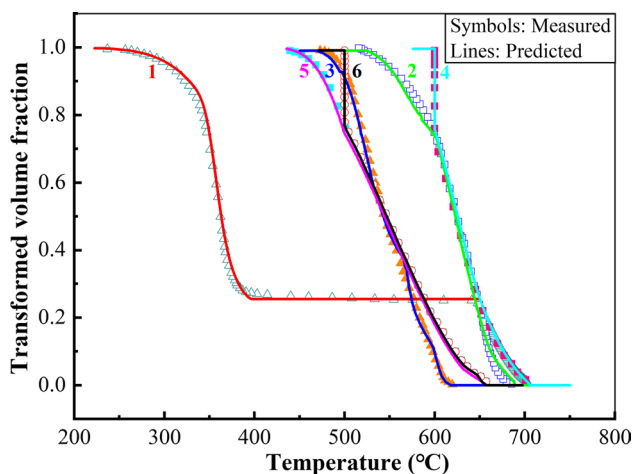


Fig. 12 The simulated and experimental transformation evolutions with temperature for the specimens cooled under different paths

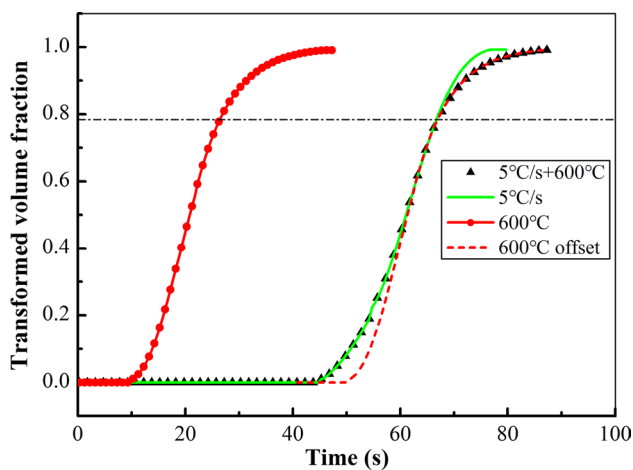


Fig. 13 Relationship between the time-dependent transformation histories for cooling path 4 and its subpaths

Figure 12 shows the simulated and experimental transformation evolutions with temperature for the specimens cooled under different paths. When the cooling rate changes, the phase transformation rate changes significantly and is no longer as smooth as the transformation at a single cooling rate. Figure 13 shows the detailed relationship between the time-dependent transformation histories (from both the calculation and experiment) for cooling path 4 in Fig. 11 and its subpaths. Obviously, the transformation curve for the two cooling rates is also an organic combination of the transformation curves at the respective cooling rates. Taking the transformation fraction at the turning point as a bridge, the latter half of the second transformation curve is offset according to the equivalent time and is combined with the first half of the first curve.

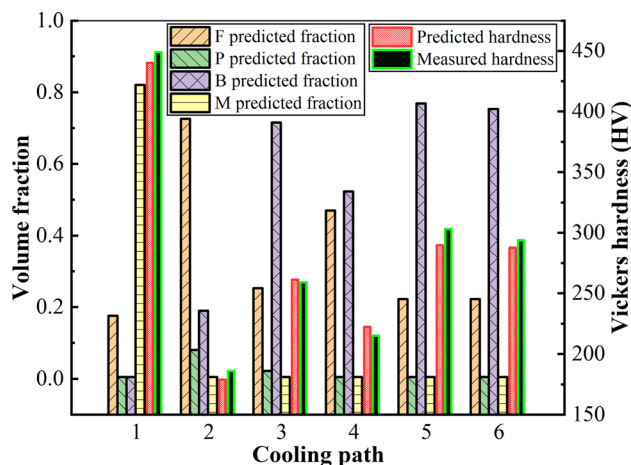


Fig. 14 The predicted volume fraction of different phases, measured and calculated Vickers hardness for specimens cooled under different paths

Figure 14 displays the predicted volume fraction of different phases and the measured and calculated Vickers hardness for specimens cooled under different paths. The hardness was calculated according to the predicted phase volume fractions. Thus, the consistency between the predicted hardness and the measured value reflects the accuracy of the predicted microconstituents indirectly.

Figure 15 shows the microconstituents for the original material and specimens cooled under paths 1, 2, 3, 4 and 5. The microstructure of the specimen under cooling path 6 is very similar to that under path 5 and therefore not presented. The microstructure showed in micrographs is basically consistent with the predicted results in Fig. 14, which further reflects the reliability of the predicted microconstituents.

In general, excellent agreement between the calculated and experimental values was observed in the transformation histories, the volume fraction microconstituents and the Vickers hardness.

4 Application

First, the kinetic model can be used with the help of programming languages, such as Python, Fortran and MATLAB, to calculate real-time volume fractions of austenite and its daughter phases, including ferrite, pearlite, bainite and martensite, under arbitrary cooling conditions.

Then, the total property Y of an arbitrary combination of phases can be calculated using a linear mixture law [1, 8] as the following:

$$Y = \sum_{i=1}^5 [X_i \cdot Y_i] \quad (13)$$

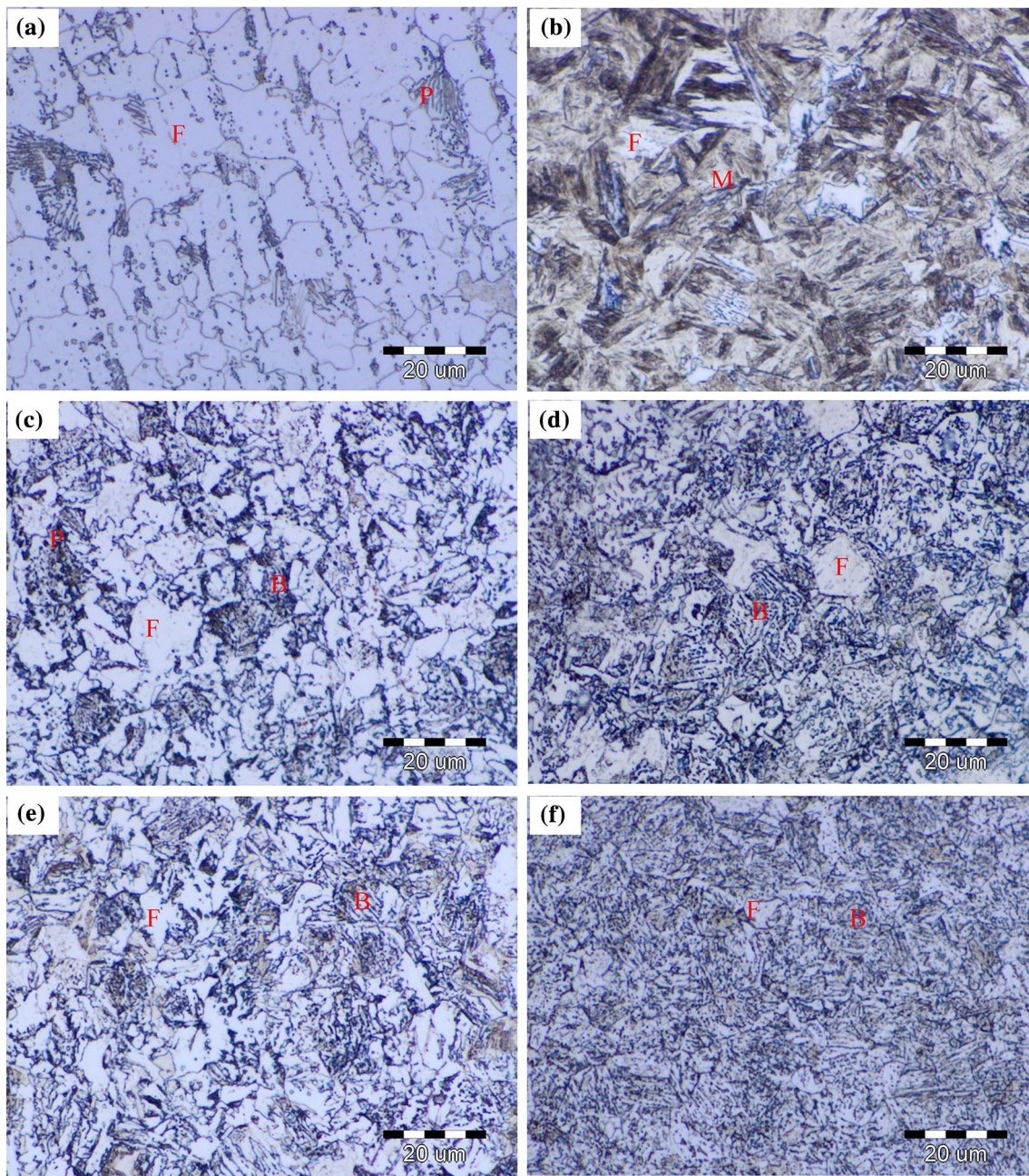


Fig. 15 Micrographs showing the microstructure for **a** the original material, specimens cooled under **b** path 1, **c** path 2, **d** path 3, **e** path 4 and **f** path 5

where Y_i is the basic property of each phase, including the physical properties (such as the density, expansion coefficient, thermal conductivity and specific heat capacity) and the mechanical properties (such as the hardness, relationships of stress and strain involving yield strength, tensile strength and elongation).

Considering the effect of the cooling rate, the total property increment ΔY can be calculated in another form:

$$\Delta Y(r_c) = \sum_{i=1}^5 [\Delta X_i \cdot f_i(r_c)] \quad (14)$$

where ΔX_i is the volume fraction increment of each phase, and $f_i(r_c)$ is a fitting function with the cooling rate for the property of individual phase.

Moreover, the kinetic model can also be implemented as a subroutine in the general FE-code LS-DYNA or in ABAQUS to simulate thermal–mechanical–microstructural coupling processes, such as hot stamping, hot forging, hot bending, heat treating or welding.

In this paper, the model was implemented as a subroutine in ABAQUS to simulate a tailored-strength hot stamping process of HSS. The moulds used in this process had both heated and cooled sides, which provide different surface temperatures and affect the cooling rate of the contacted blank. As a consequence, the parts hot stamped by these moulds exhibited different microstructure components and mechanical properties.

Figure 16 shows the temperature distribution on the blank just after quenching in the moulds. The temperature on one side of the part was greater than M_s , while the temperature on the other side was less than M_f , indicating that the cooling rates on both sides of the part were quite different during the in-mould cooling process.

Figure 17 shows the predicted bainite and martensite distributions of the part at different stages of hot stamping; and Fig. 18 displays the simulated Vickers hardness distribution on the obtained part. The microstructure comprises mainly bainite on one side of the final part (low-strength side) while fully martensite on the other side (high-strength side). After

Fig. 16 Temperature distribution on the blank just after cooled in-moulds (in °C)

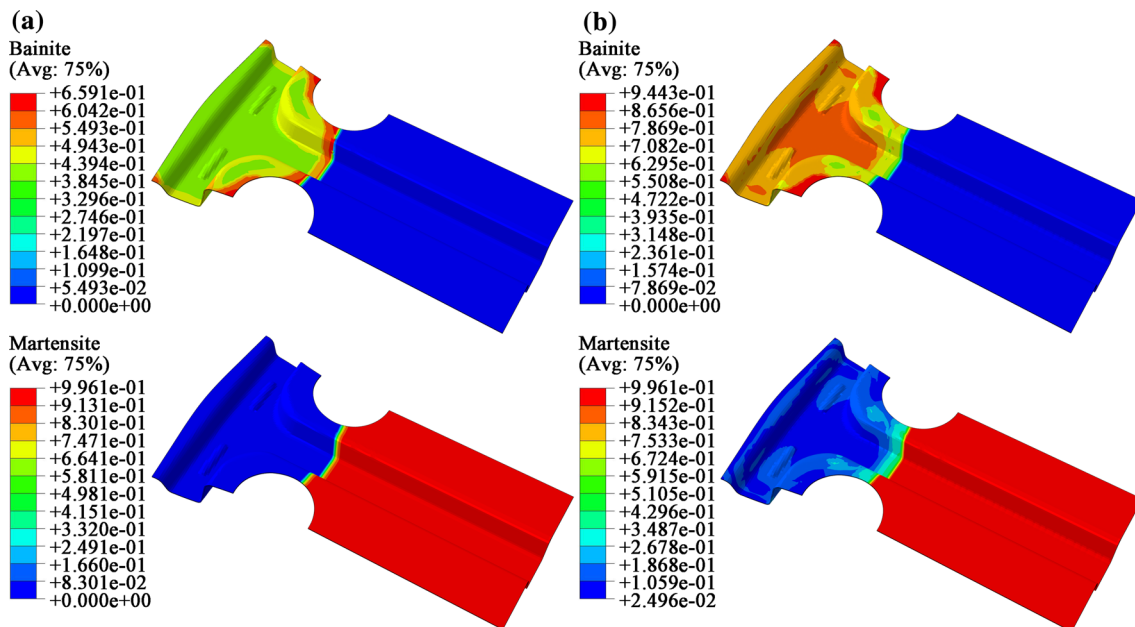
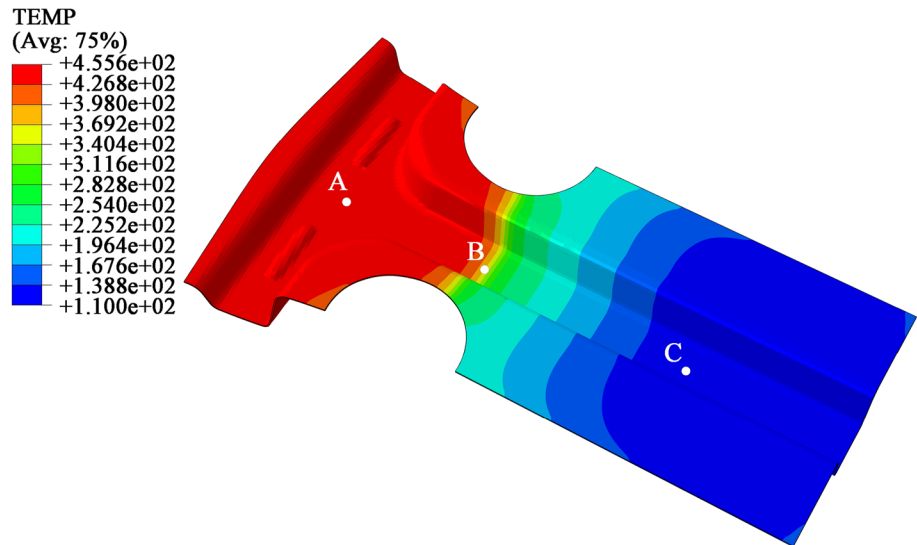


Fig. 17 The predicted bainite and martensite distributions of the part at different stages of hot stamping: **a** after cooled in-moulds and **b** after cooled in-air

Fig. 18 The predicted Vickers hardness distribution on the obtained part

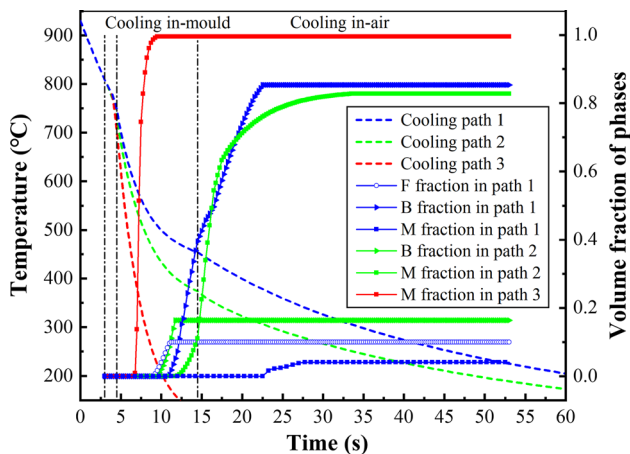
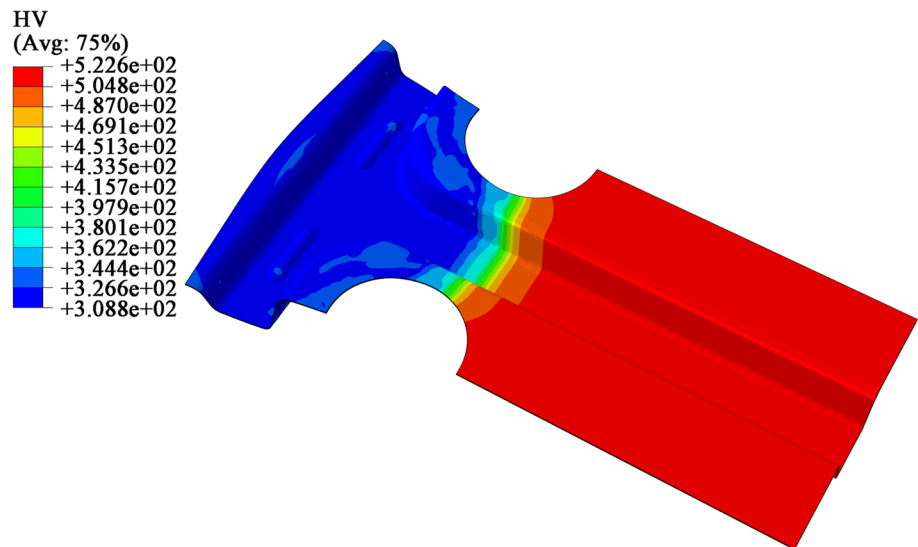


Fig. 19 The cooling paths and microstructure evolutions of several key points on the blank

the in-mould cooling process, the martensite fraction was greater than 95% on the high-strength side; the bainite fraction was approximately 40% on the low-strength side, and 50% of the austenite remains untransformed. The retained austenite continues to decompose during the in-air cooling process resulting in a bainite fraction of 85% on the low-strength side of the final part. The hardness was close to 310 HV on the low-strength side of the part yet as high as 515 HV on the high-strength side. Compared with the 180 HV of the as-received steel, the high-strength side was obviously hardened, and, relatively speaking, the low-strength side was hardened slightly.

Figure 19 shows the cooling paths and microstructure evolutions of several key points on the blank corresponding to the marks in Fig. 16. The types of daughter phases can be confirmed by combining the CCT curves in Fig. 7; however, the kinetic model for phase transformation must be

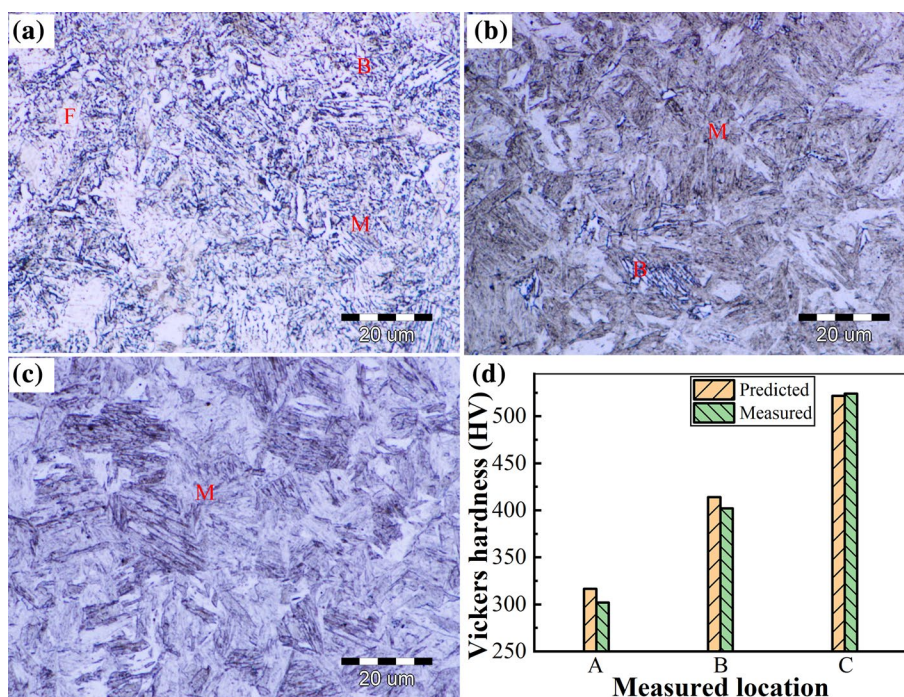
used to calculate the specific volume fraction of each transformation. Figure 20 shows the microconstituents and corresponding Vickers hardness of these points. As expected, the microstructure shown in the micrographs is basically consistent with the predicted results in Fig. 19, and the predicted hardness is in good agreement with the measured data. Therefore, the reliability and practicality of the model have been further confirmed, and the model can be used to simulate the microstructure and mechanical properties of HSS in a hot stamping process.

5 Discussion and Conclusion

In this study, the non-isothermal phase transformation kinetics of BR1500HS steel were developed based on the JMAK and Kamamoto models. The kinetics of both the diffusional and diffusionless transformations can be written in a unified form. The proposed kinetic model is slightly complicated, and large amounts of test data were needed to identify the kinetic parameters. However, the model can describe the phase transformation kinetics under TTT or CCT cooling conditions with good accuracy.

A process of calculating the volume fraction for phase transformations under arbitrary cooling conditions was proposed. For diffusional transformations, an improved Scheil additivity rule was used to calculate the incubation time under arbitrary cooling conditions based on the TTT and CCT data. The influence of the cooling rate on the martensite transformation was caused by the volume fraction of the diffusional transformations indirectly and equivalently. Then, the ability of the kinetic model to accurately predict the transformation histories and hardness of HSS under arbitrary cooling conditions was verified.

Fig. 20 Micrographs showing the microstructure for **a** point A, **b** point B and **c** point C, with **d** the corresponding Vickers hardness



Moreover, the modelling method used for the phase transformation of HSS in this paper can also be applied to other materials. Based on the property (e.g., hardness) test data for each phase, the predicted microstructures can be used to further predict the property of the mixed phases.

While there is no consideration of the stress and strain in the model, this deficiency can be improved by using additional test data by applying the same research method suggested in the present work.

Acknowledgements This project was supported by the National Natural Science Foundation of China (Grant No. 51405149).

References

1. P. Åkerström, G. Bergman, M. Oldenburg, Numerical implementation of a constitutive model for simulation of hot stamping. *Model. Simul. Mater. Sci. Eng.* **15**(2), 105–119 (2007)
2. G. Georgiadis, A.E. Tekkaya, P. Weigert, S. Horneber, P.A. Kuhnleal, Formability analysis of thin press hardening steel sheets under isothermal and non-isothermal conditions. *Int. J. Mater. Form.* **10**(3), 1–15 (2016)
3. H. Karbasian, A.E. Tekkaya, A review on hot stamping. *J. Mater. Process. Technol.* **210**(15), 2103–2118 (2010)
4. P. Hippchen, A. Lipp, H. Grass, P. Craighero, M. Fleischer, M. Merklein, Modelling kinetics of phase transformation for the indirect hot stamping process to focus on car body parts with tailored properties. *J. Mater. Process. Technol.* **228**(8), 59–67 (2016)
5. R. George, A. Bardelcik, M.J. Worswick, Hot forming of boron steels using heated and cooled tooling for tailored properties. *J. Mater. Process. Technol.* **212**(11), 2386–2399 (2012)
6. K. Omer, R. George, A. Bardelcik, M. Worswick, S. Malcolm, D. Detwiler, Development of a hot stamped channel section with axially tailored properties—experiments and models. *Int. J. Mater. Form.* **11**(1), 1–16 (2017)
7. B.A. Hay, B. Bourouga, C. Dessain, Thermal contact resistance estimation at the blank/tool interface: experimental approach to simulate the blank cooling during the hot stamping process. *Int. J. Mater. Form.* **3**(3), 147–163 (2010)
8. P. Åkerström, M. Oldenburg, Austenite decomposition during press hardening of a boron steel—computer simulation and test. *J. Mater. Process. Technol.* **174**(1), 399–406 (2006)
9. H.H. Bok, S.N. Kim, D.W. Suh, F. Barlat, M.G. Lee, Non-isothermal kinetics model to predict accurate phase transformation and hardness of 22MnB5 boron steel. *Mater. Sci. Eng., A* **626**, 67–73 (2015)
10. W.A. Johnson, R.F. Mehl, Reaction kinetics in processes of nucleation and growth. *Trans. Am. Inst. Min. Metall. Eng.* **135**, 416–458 (1939)
11. M. Avrami, Kinetics of phase change. III: granulation, phase change and microstructure. *J. Chem. Phys.* **9**(2), 177–184 (1941)
12. A.N. Kolmogorov, On the statistical theory of metal crystallization. *Izv. Akad. Nauk. SSSR Ser. Mat.* **3**, 355–359 (1937)
13. Kirkaldy J.S., Venugopalan D. Prediction of microstructure and hardenability in low-alloy steels, in *Phase Transformation in Ferrous Alloys*, ed. by A.R. Marder, J.I. Goldstein, 1983, pp. 125–148
14. J.W. Cahn, The kinetics of grain boundary nucleated reactions. *Acta Metall.* **4**(5), 449–459 (1956)
15. M. Umemoto, N. Nishioka, Prediction of hardenability from isothermal transformation diagrams. *J. Heat. Treat.* **2**(2), 130–138 (1981)
16. F. Liu, F. Sommer, E.J. Mittemeijer, An analytical model for isothermal and isochronal transformation kinetics. *J. Mater. Sci.* **39**(5), 1621–1634 (2004)
17. A. Pohjonen, M. Somani, D. Porter, Modelling of austenite transformation along arbitrary cooling paths. *Comput. Mater. Sci.* **150**, 244–251 (2018)

18. M.V. Li, D.V. Niebuhr, L.L. Meekisho, D.G. Atteridge, A computational model for the prediction of steel hardenability. *Metall. Mater. Trans. B* **29**(3), 661–672 (1998)
19. N. Saunders, Z. Guo, X. Li, A.P. Miodownik, J.P. Schillé, *The Calculation of TTT and CCT diagrams for General Steels*. Sente Software Ltd, 2004
20. S.J. Lee, E.J. Pavlina, C.J.V. Tyne, Kinetics modeling of austenite decomposition for an end-quenched 1045 steel. *Mater. Sci. Eng., A* **527**(13), 3186–3194 (2010)
21. D.P. Koistinen, R.E. Marburger, A general equation prescribing the extent of the austenite-martensite transformation in pure iron-carbon alloys and plain carbon steels. *Acta Metall.* **7**(1), 59–60 (1959)
22. C.L. Magee, The nucleation of martensite, in *Phase Transformations*, ed. by H.I. Aaronson, V.F. Zackay, ASM International, 1970, pp. 115–156
23. K. Tanaka, A thermomechanical sketch of shape memory effect: one-dimensional tensile behavior. *Res. Mech.* **18**, 251–263 (1986)
24. S.J. Lee, Y.K. Lee, Finite element simulation of quench distortion in a low-alloy steel incorporating transformation kinetics. *Acta Mater.* **56**(7), 1482–1490 (2008)
25. R.F. Hehemann, K.R. Kinsman, H.I. Aaronson, A debate on the bainite reaction. *Metall. Trans.* **3**(5), 1077–1094 (1972)
26. H.K.D.H. Bhadeshia, D.V. Edmonds, The bainite transformation in a silicon steel. *Metall. Trans. A* **10**(7), 895–907 (1979)
27. F.G. Caballero, M.K. Miller, C. Garcia-Mateo et al., New experimental evidence of the diffusionless transformation nature of bainite. *J. Alloy. Compd.* **577**(5), S626–S630 (2013)
28. A. Borgenstam, M. Hillert, J. Ågren, Metallographic evidence of carbon diffusion in the growth of bainite. *Acta Mater.* **57**(11), 3242–3252 (2009)
29. Z.C. Liu, H.Y. Wang, H.P. Ren, Shear-diffusion conformity mechanism of bainite transformation. in *Heat Treatment of Metals*, 2006
30. S. Kamamoto, T. Nishimori, S. Kinoshita, Analysis of residual stress and distortion resulting from quenching in large low-alloy steel shafts. *Met. Sci. J.* **1**(10), 798–804 (1985)
31. W. Piekarska, M. Kubiak, Z. Saternus, Numerical modelling of thermal and structural strain in laser welding process/Modelowanie Numeryczne Odształceń Ciepłych I Strukturalnych W Procesie Spawania Technika Laserowa. *Arch. Metall. Mater.* **57**(4), 1219–1227 (2012)
32. F. Liu, F. Sommer, C. Bos et al., Analysis of solid state phase transformation kinetics: models and recipes. *Metall. Rev.* **52**(4), 193–212 (2007)
33. J. Rohde, A. Jeppsson, Literature review of heat treatment simulations with respect to phase transformation, residual stresses and distortion. *Scand. J. Metall.* **29**(2), 47–62 (2010)
34. E.B. Hawbolt, B. Chau, J.K. Brimacombe, Kinetics of austenite-ferrite and austenite-pearlite transformations in a 1025 carbon steel. *Metall. Trans. A* **16**(4), 565–578 (1985)
35. M. Lusk, H. Jou, On the rule of additivity in phase transformation kinetics. *Metall. Mater. Trans. A* **28**(2), 287–291 (1997)
36. Y.T. Zhu, T.C. Lowe, Application of, and precautions for the use of, the Rule of additivity, in phase transformation. *Metall. Mater. Trans. B* **31**(4), 675–682 (2000)
37. M. Naderi, A. Saeed-Akbari, W. Bleck, The effects of non-isothermal deformation on martensitic transformation in 22MnB5 steel. *Mater. Sci. Eng., A* **487**(1), 445–455 (2008)
38. M. Nikraves, M. Naderi, G.H. Akbari, Influence of hot plastic deformation and cooling rate on martensite and bainite start temperatures in 22MnB5 steel. *Mater. Sci. Eng., A* **540**(4), 24–29 (2012)
39. H.C. Kang, B.J. Park, H.J. Ji et al., Determination of the continuous cooling transformation diagram of a high strength low alloyed steel. *Met. Mater. Int.* **22**(6), 949–955 (2016)
40. T.T. Pham, E.B. Hawbolt, J.K. Brimacombe, Predicting the onset of transformation under noncontinuous cooling conditions: Part II: application to the austenite pearlite transformation. *Metall. Mater. Trans. A* **26**(8), 1993–2000 (1995)
41. J.L. Lee, Y.T. Pan, K.C. Hsieh, Assessment of ideal TTT diagram in C–Mn steels. *Mater. Trans.* **39**(1), 196–202 (1998)
42. J.S. Kirkaldy, Prediction of alloy hardenability from thermodynamic and kinetic data. *Metall. Trans.* **4**(10), 2327–2333 (1973)
43. A. Malakizadi, S. Hatami, L. Nyborg, Simulation of cooling behavior and microstructure development of PM steels. *Int. J. Oncol.* **37**(4), 829–835 (2010)
44. K. Omer, R. George, A. Bardelcik, M. Worswick, S. Malcolm, D. Detwiler, Development of a hot stamped channel section with axially tailored properties—experiments and models. *Int. J. Mater. Form.* **11**(1), 1–16 (2017)